Research Article Vol. 33, No. 3 / 10 Feb 2025 / Optics Express 6080

Optics EXPRESS

Spectral fingerprinting of aqueous glucose with ultra-broadband vibrational sum-frequency generation spectroscopy at bio-relevant low concentration

CHENG LUO,[1,2] MAHESH NAMBOODIRI,[1] MICHAEL SCHULZ,[3] ROBERT RIEDEL,[3] MARK J. PRANDOLINI,[3,4] AND TIM LAARMANN[1,2,5]

[1] *Deutsches Elektronen-Synchrotron DESY, Notkestraße 85, 22607 Hamburg, Germany*
[2] *The Hamburg Centre for Ultrafast Imaging CUI, 22761 Hamburg, Germany*
[3] *Class 5 Photonics GmbH, Notkestraße 85, 22607 Hamburg, Germany*
[4] *Universität Hamburg, Institut für Experimentalphysik, Luruper Chaussee 149, 22761 Hamburg, Germany*
[5] *tim.laarmann@desy.de*

Abstract: Vibrational modes of glucose spanning from 900 to 1400 cm^{-1} in the molecular fingerprint region have been traced by means of vibrational sum-frequency generation spectroscopy in aqueous solution as a function of glucose concentration. The high sensitivity is enabled by a 200 kHz few-cycle mid-infrared optical parametric chirped-pulse amplifier (OPCPA). The OPCPA generates broadband pulses (from 7 to 11 µm) centered at 9 µm with 114 fs pulse duration, at a high average power of 245 mW and high pulse energy of 1.2 µJ. The achieved performance of the spectrometer is benchmarked by probing the carbon-oxygen bond stretching mode at 1035 cm^{-1} using a biologically relevant low sample concentration of 10 mM.

1. Introduction

Monitoring blood glucose levels is a critical task in the prevention and management of diabetes. Traditional testing methods such as finger pricking can be uncomfortable and there are variations in blood sugar readings due to different test strips. Therefore, there is growing interest in the development of sensitive and accurate noninvasive glucose monitoring techniques. In recent years, infrared vibrational spectroscopy of biofluids [1] has emerged as a promising approach, because abundant information on important biomolecules is available in the mid-infrared (MID-IR) range from 6 to 16 µm, which corresponds to 625-1667 cm^{-1} in wavenumber, also known as the molecular fingerprint region. Specifically, the stretching modes of carbon-oxygen bonds between 1000 and 1200 cm^{-1} have shown a high sensitivity to glucose concentration [2]. Typically, a concentration of $\approx$ 50 mM is prepared in cell cultures to mimic diabetic conditions [3], which is not detectable with standard Fourier-transform infrared (FTIR) spectroscopy [4].

Using quantum cascade lasers [2], researchers have observed a linear relationship between the absorption band at 1035 cm^{-1} and glucose concentration down to 5.5 mM, a range that closely aligns with human blood sugar levels of 4-11 mM. Raman spectroscopy has demonstrated the ability to detect even lower concentrations of 1 mM by targeting the bending mode of C-O-H bonds at 1125 cm^{-1} [5]. Because of light absorption by nonglucose components, the Raman glucose peak is often a weak signal in vivo. To enhance the detection capabilities of Raman spectroscopy, techniques such as surface-enhanced Raman scattering [6] and graphene-enhanced Raman scattering [7] have been employed, which significantly increased signal strength and

#544862 https://doi.org/10.1364/OE.544862
Journal © 2025 Received 15 Oct 2024; revised 24 Jan 2025; accepted 28 Jan 2025; published 6 Feb 2025

reduced acquisition time. Moreover, to address challenges such as fluorescence background interference, which is caused by laser irradiation, coherent Raman methodologies like coherent anti-Stokes Raman scattering [8] and stimulated Raman scattering [9] have been utilized, which offered fluorescence background-free glucose spectra that can be recorded in a phenomenal 0.6 s integration time. Ultrashort MID-IR pulses offer even more opportunities in glucose sensing. For example, sub-cycle MID-IR pulses allow for recording four-wave difference-frequency generation spectra of the free induction decay of the solute [10]. Measuring the up-converted visible spectrum using standard Si-based detectors provides background-free absorption information of aqueous glucose in the fingerprint and functional group regions from 500 to 4500 cm^{-1} with single-shot capability. Thereby, the authors of reference [10] recorded absorption spectra of glucose in the electronic ground state at a concentration of 50 mM with high efficiency. Recently, MID-IR field-resolved spectroscopic studies have pushed the concentration limit even further and reached concentration levels down to 0.1 mM [11]. Besides, enhanced selective excitation of ground-state vibrational modes, femtosecond MID-IR pulses could be used to identify different cellular components by means of hyperspectral imaging [12].

As a powerful analytical method, which is in the focus of the present study, vibrational sum-frequency generation (VSFG) spectroscopy involves the combination of infrared and visible laser beams with a power density of I_{VIS} and I_{IR}, respectively. When the angular frequency of the infrared beam ω_{IR} resonantly excites a vibrational transition $\nu_0 \rightarrow \nu_1$ within a molecule and the visible beam ω_{VIS} interacts with the vibration as it decays back to its ground state, the scheme enables the extraction of vibrational information by detecting the emitted photons from the molecule at the sum frequency ω_{SFG}, denoted as $\omega_{\mathrm{SFG}} = \omega_{\mathrm{IR}} + \omega_{\mathrm{VIS}}$. In this nonlinear process, the spectral bandwidth of the visible beam determines the spectral resolution in the measured vibrational spectrum. The VSFG process is illustrated by Fig. 1 and Eq. (1) describes the SFG signal strength that can be recorded in reflection, transmission and scattering detection mode [13].

$$\begin{aligned} I_{\mathrm{SFG}} &\propto |\tilde{\mathbf{P}}(\omega_{\mathrm{SFG}})|^2 \\ &\propto |\chi^{(2)}_{\mathrm{NR}} + \sum_q \chi^{(2)}_{\mathrm{R}q} \mathrm{e}^{i\gamma_q} + \chi^{(3)}\mathrm{E}_{\mathrm{DC}}|^2 \mathrm{sinc}^2\left(\frac{L\Delta\mathbf{k}}{2}\right) L^2 I_{\mathrm{VIS}} I_{\mathrm{IR}}, \\ &\text{where } \chi_{\mathrm{R}q}{}^{(2)}_{\mathrm{i,j,k}} \propto \frac{\alpha_{\mathrm{i,j}} \cdot \mu_{\mathrm{k}}}{\omega_q - \omega_{\mathrm{IR}} - i\Gamma_q}. \end{aligned} \tag{1}$$

Here, $\chi^{(2)}_{\mathrm{NR}}$ and $\chi^{(2)}_{\mathrm{R}q}$ present the nonresonant and resonant part of the second-order nonlinear susceptibility, and γ_q is the relative phase of the q_{th} vibrational mode characterized by bond-specific vibrational states ν. In some cases, third-order contributions $\chi^{(3)}$ will also show up, if there is a net electrical field E_{DC} within the system of interest, e.g., ionic species adsorb at the water surface [14]. The component involving the sinc function is the synchronization factor, which accounts for the phase matching between the incoming and the emitted SFG beams ($\Delta\mathbf{k} = \mathbf{k}_{\mathrm{SFG}} - \mathbf{k}_{\mathrm{VIS}} - \mathbf{k}_{\mathrm{IR}}$) in the specified dimension (L) as the beams propagate through the sample. The activity of VSFG is primarily related to infrared activity (dipole moment change), but the VSFG signal is generated by the molecular nonlinear polarizability. Furthermore, the nonlinear susceptibility $\chi^{(2)}$ essentially includes contributions from the molecular polarizability tensor. In other words, the generation of a VSFG signal primarily depends on infrared activity, while Raman activity (polarizability change) acts as an enhancement factor but is not a necessary condition. Mathematically, the rank-3 tensor $\chi^{(2)}_{Rq}$ is a direct product of the Raman transition polarizability $\alpha_{\mathrm{i,j}}$ and the IR transition dipole moment μ_{k} where the vibration is characterized by the resonant frequency ω_q and the natural line width of the transition Γ_q [15]. Eq. (1) implies that VSFG is only observable in a medium where centrosymmetry is broken, such as surfaces, interfaces, and even the analysis of sub-monolayers of interfacial molecules has been demonstrated [16–18], making VSFG a valuable nonlinear optical tool for surface- and interface-specific vibrational studies. In general, the spatial distribution (probing depth) of SFG-active noncentrosymmetric area at the interface within the coherence length of the propagating beams is defined by the synchronization factor and influences the VSFG spectral features and intensities.

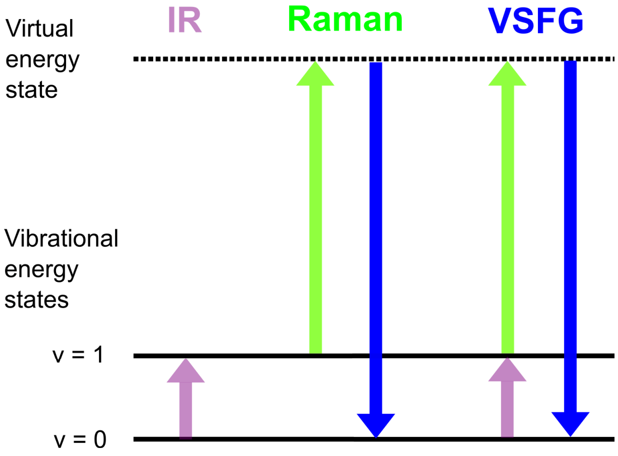

Fig. 1. Illustration of vibrational sum-frequency generation (VSFG) with contributions arising from IR absorption of vibrational modes characterized by bond-specific vibrational energy states $v = 0, 1$. (horizontal lines) and Raman scattering from a virtual energy state of the molecule (horizontal dotted line).

Since 1999, researchers have utilized VSFG spectroscopy to investigate the vibrational characteristics of glucose within the spectral range of 2800 to 3000 cm^{-1} [19–21]. Notably, there is no published VSFG study on glucose between 1000 and 1200 cm^{-1}, which would give characteristic vibrational fingerprints in aqueous environments. Obviously, there are challenges in high-power laser development in the spectral fingerprint region. Typical MID-IR generation schemes via difference-frequency generation (DFG) involve $AgGaS_2$ or GaSe crystals. However, due to the high linear and nonlinear absorption, these crystals need to be pumped at wavelengths close to 2 µm. Therefore, often-used high-power Yb:YAG lasers operating at 1 µm require an additional conversion step towards 2 µm, which results in low over-all conversion efficiency. The power scaling of MID-IR few-cycle laser systems has been improved by recent advances in crystal growth technology [22], particularly through the superior optical properties of the $LiGaS_2$ (LGS) crystal, which can be pumped directly at 1 µm [23]. Applied in a single OPA stage, broadband pulses centered around 1180 cm^{-1} with high output power of 48 mW have been demonstrated [24]. Following this strategy, our home-built 200 kHz OPCPA system (White Dwarf HE DFG prototype) provides a pulse energy of 1.2 µJ and average power of 245 mW centered around 1100 cm^{-1} [25]. This development prepared the ground for observing distinct glucose absorption bands in VSFG spectroscopy at physiologically relevant low concentrations in the present study. As far as we know, there has been no 200 kHz VSFG study on air/liquid interfaces reported in the literature. Among the very few studies using a somewhat lower pulse repetition rate of 100 kHz, we would like to highlight the work by Cao et al., who published broadband VSFG spectra with extremely high spectral resolution of 0.6 cm^{-1} and excellent line shape from an air/dimethyl sulfoxide aqueous solution interface [26], as well as the work by Heiner et al. presenting high-resolution (3 cm^{-1}), low-noise vibrational spectra of lipid monolayers on CaF_2 [24]. The latter study used a very compact setup also based on LGS pumped directly at 1 µm. Thereby, the authors could omit optical parametric amplification in nonlinear oxide materials followed by DFG between the signal and the idler in a non-oxide material, which typically limited the pump to MID-IR energy conversion efficiency to $\approx 0.5\,\%$ [27–29]. Inspired by these works, we have developed a VSFG spectroscopy setup that leverages two complementary operation modes of the MID-IR OPCPA, a wide wavelength scanning range from 800 to 2500 cm^{-1} and an ultra-broadband (few-cycle pulse) from 900 to 1400 cm^{-1}. In the present experiment, the narrowband visible and the ultra-broadband MID-IR laser pulses are temporally and spatially overlapping at the sample surface [30]. The recorded data demonstrate the system's capability to obtain ultra-broadband MID-IR absorption spectra from organic samples at physiologically relevant low concentrations without tuning the central wavelength of the MID-IR beam.

2. Methods

2.1. MID-IR OPCPA

The optical configuration of the MID-IR OPCPA is explained in more detail elsewhere [25]. In brief, the system is driven by a total of 40 W output at 200 kHz repetition rate from a commercial Yb:YAG InnoSlab (Amphos A8000) laser system, equivalent to a pulse energy of 200 µJ. The total energy is distributed to three branches: White-light generation (WLG), second-harmonic generation (SHG), and the pump for difference-frequency generation (DFG). A portion of 8 µJ is directed towards generating the signal pulse through the WLG process within an undoped YAG crystal of 10 mm length. In order to stretch the duration of the signal pulse, either positive or negative group delay dispersion (GDD) can be introduced, leading to a versatile design of a MID-IR OPCPA laser system, featuring two complementary operation modes. The scenario of the positively chirped pulse via SF11 glass was demonstrated in our previous work [25], providing a wavelength-tunable MID-IR source (from 4.2 to 11 µm) at ≈ 1 ps pulse width. In the present work, by dealing with the negatively chirped signal, the custom-made chirped mirrors (CM) introduce a total GGD of -11000 fs^2 (20 reflections). Another portion of 26 µJ is directed towards a 1 mm thick β-Barium Borate (BBO) (type I phase-matching) for the SHG pump of non-collinear OPA (NOPA). The NOPA delivers a pulse energy of ≈ 2 µJ in the wavelength range of 1150 - 1200 nm, utilized as a seed for the DFG stage. Following the NOPA setup, the remaining pulse energy of the pump ≈155 µJ is used as the pump in the final DFG stage consisting of an LGS crystal (type II phase-matching in the XY plane, $\theta = 90°$; $\phi = 37.5°$). After the MID-IR idler generation, a straightforward beam separator takes advantage of the greater divergence in the long-wavelength idler. By combining a two-inch concave mirror with a center 4 mm hole coated with gold and a protected gold convex mirror, a part of the MID-IR can be easily separated and collimated. The central hole allows the high-power pump and signal pulses, along with ≈ 65 % of the MID-IR idler, to pass through. After the separation of the MID-IR from the pump, a 6 mm thick ZnSe bulk acts as a temporal pulse width compressor to compensate remaining positive GDD in the MID-IR pulses and a long-pass filter to block any remaining signal beam before entering the ultra-broadband VSFG spectroscopic setup.

The spectral properties of MID-IR idler pulses are characterized by a home-built FTIR, as depicted in Fig. 2(a). The FTIR has spectral resolution of 59 GHz, which corresponds to 2.0 cm^{-1} in wavenumbers [31]. The measured MID-IR spectra can be adjusted within the range of 7.8 to 10.2 µm by tuning the central wavelength of the signal in the NOPA. The broad spectrum at a central wavelength of 9 µm has an average power of around 240 mW corresponding to ≈ 1.2 µJ at 200 kHz. It is important to note that the LGS transmission near 9 µm is only about 20 % [32], which is evident as a dip in the recorded FTIR spectrum. Another crucial factor of the spectral profile is the phase-matching angle θ of the LGS crystal. To cover a broad spectral range with a Gaussian-like envelope well-suited for VSFG spectroscopy and temporal pulse compression, the spectrum at a central wavelength of 9 µm is optimized by fine-tuning the phase-matching angle of the LGS crystal. The generated broadband MID-IR pulses are characterized in time domain by a commercial interferometric autocorrelator (APE). Fig. 2(b) shows the second-order interferometric autocorrelation trace. The envelope of the constructive interferences has the characteristic peak-to-background ratio of 8 to 1 for mode-locked laser pulses and the Gaussian fit to the data gives the characteristic 3 to 1 ratio known from conventional intensity autocorrelation measurements. The shortest autocorrelation width of 168 fs reveals a pulse width τ_p = 114 fs corresponding to 3.8 optical cycles at a central wavelength of 9 µm, which makes this laser source also an ideal tool for advanced fs pulse-shaping applications in the MID-IR [31].

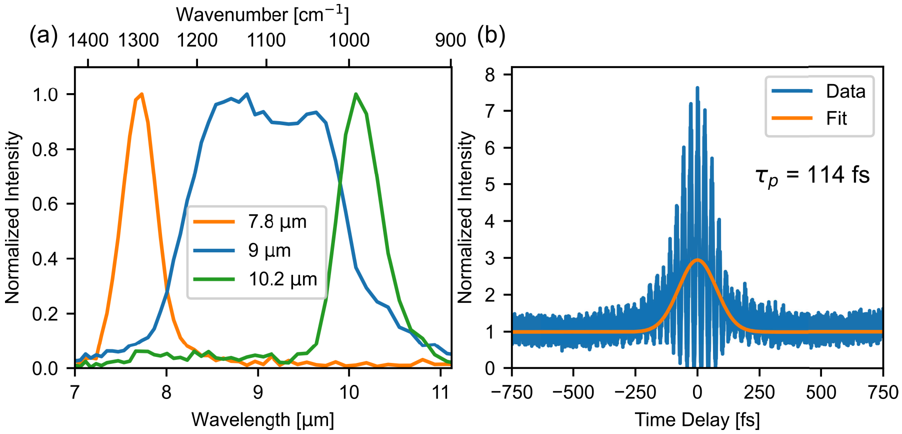

Fig. 2. (a) Wavelength-tunable MID-IR pulse spectra generated from the negatively chirped signal NOPA scheme at 7.8 µm, 9 µm, and 10.2 µm central wavelength. (b) The second-order interferometric autocorrelation trace (blue data points) of the broadband, 9 µm MID-IR pulse fitted with a Gaussian function (orange line) reveals a pulse duration τ_p = 114 fs (for details, see the main text)

2.2. Ultra-broadband VSFG setup

Following the DFG stage, the MID-IR beam is maintained at P-polarization as it was initially generated, and the power can be arbitrarily adjusted by rotating a wire-grid polarizer, which not only transmits the P-polarized MID-IR beam but also eliminates any light leakage from the OPCPA. The maximum MID-IR power of 120 mW is focused on the sample position using a ZnSe lens, resulting in an intensity of ≈ 1.5 GW/cm^2 according to calculations. After setting the MID-IR to P-polarization, the VIS should be fixed at S-polarization for the strong response of the S-polarized SFG, as calculated by the Fresnel factors [33]. An S-polarized 515 nm beam generated by the SHG from the pump laser pulses provides a pulse duration on the order of ≈ 1 ps. It is important to clean the VIS beam with a bandpass filter (BPF) to remove unwanted light from the previous DFG stage. Once the beam is filtered, focusing 1 W of power on the sample position results in an intensity of ≈ 7 GW/cm^2. The angle of incidence is 45° and 53° relative to the surface normal for the MID-IR and the VIS beam, respectively. To improve the collection of scattered SFG light from solid samples with rough surfaces, such as cellulose and glucose pellets, a lens with a short focal length of 30 mm is used. The reflected SFG beam is directed into the detection branch by means of a flip mirror (FM). In the case of a highly transparent sample, such as aqueous glucose in a liquid cell, the transmitted SFG beam can be measured separately by flipping the mirror. The Glan-Thompson polarizer selectively transmits the S-polarized SFG, while the BPF blocks the 515 nm beam and allows the SFG beam in the spectral region of interest from 480 to 492 nm to transmit. Finally, a lens placed before the spectrometer focuses the light onto a slit width of 500 µm to enhance the spectral resolution and transmission intensity of the SFG. After directing the light into the spectrometer, the frequencies of SFG beam are dispersed by a 1800 l/mm grating of the spectrograph and then captured with a CCD camera, which features a 2048 × 512 array of 13.5 µm sized pixels and is equipped with thermoelectric cooling down to -50 °C for exceptional performance. The spectral bandwidth of the visible beam (0.9 nm) determines the resolution (32 cm^{-1}) of the VSFG spectrometer shown in Fig. 3.

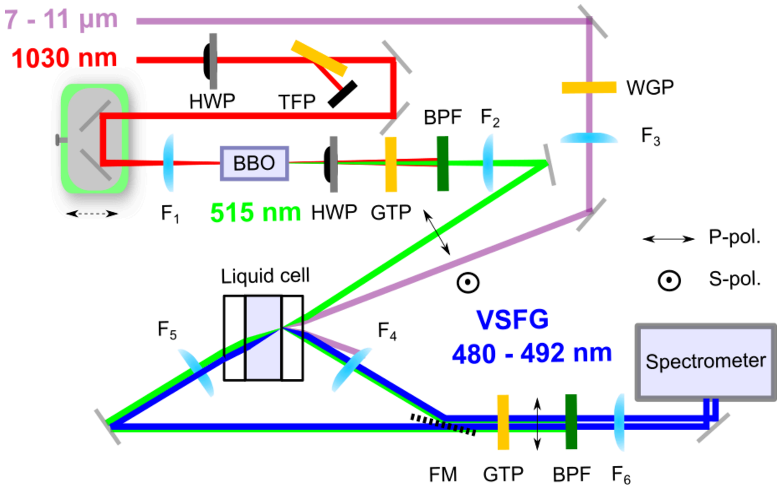

Fig. 3. Schematic of the ultra-broadband VSFG spectroscopy setup. HWP: half-wave plate, TFP: thin film polarizer, BBO: BaB_2O_4, GTP: Glan-Thompson polarizer, WGP: wire-grid polarizer, BPF: bandpass filter, Lenses: $F_1 = 150$ mm, $F_2 = 200$ mm, $F_3 = 200$ mm, F_4 : 30 mm, F_5 : 75 mm, F_6 : 150 mm, FM: flip mirror.

3. Results

3.1. *Sum-frequency phonon spectroscopy on α-quartz for VSFG alignment*

We first measure the SFG spectrum from a 5 mm thick z-cut α-quartz crystal, which has been demonstrated to show strong zone-center optical phonon absorption peaks at 1065 and 1160 cm^{-1} [34]. At somewhat higher photon energies (2000-4000 cm^{-1}) quartz shows a flat spectral response and is typically used as an absolute intensity and phase standard in SFG vibrational spectroscopy in this spectral range [35]. In the present work, the quartz sample allows for easy alignment and first calibration of the VSFG spectrometer providing a strong resonance-enhanced SFG signal. Once the signal is properly directed onto the CCD camera, the measurement can proceed under optimized experimental conditions by switching from the quartz reference to the samples of interest. Fig. 4(a) displays the well-known SFG-response spectrum from quartz measured in the reflection mode of signal detection. The excitation energy of characteristic optical phonon modes of the α-quartz crystal lies well within the MID-IR pulse spectrum.

3.2. *Spectral calibration of the setup using cellulose pellets*

Before measuring solid glucose and glucose at low concentration in solution, it is advisable to measure a well-characterized organic test sample showing a more complex SFG response compared to the quartz phonon modes to showcase the capabilities of the VSFG spectrometer. Also, its fine calibration (typically below ±10 cm^{-1} accuracy) using sharp spectral features is essential. Cellulose is well suited for this task. In crystalline form is has been investigated in the MID-IR fingerprint region by Kim et al.[13]. Cellulose is a linear polysaccharide comprising thousands of glucose units and is mostly located in cell walls of plants serving as an essential structural component. Their spectroscopic results using IR, Raman, and SFG techniques provide details on its structure, chain orientation, and vibrational modes [36,37]. Microcrystalline cellulose powder with a particle size of ≈ 50 µm (Sigma-Aldrich) is hand-pressed into a pellet

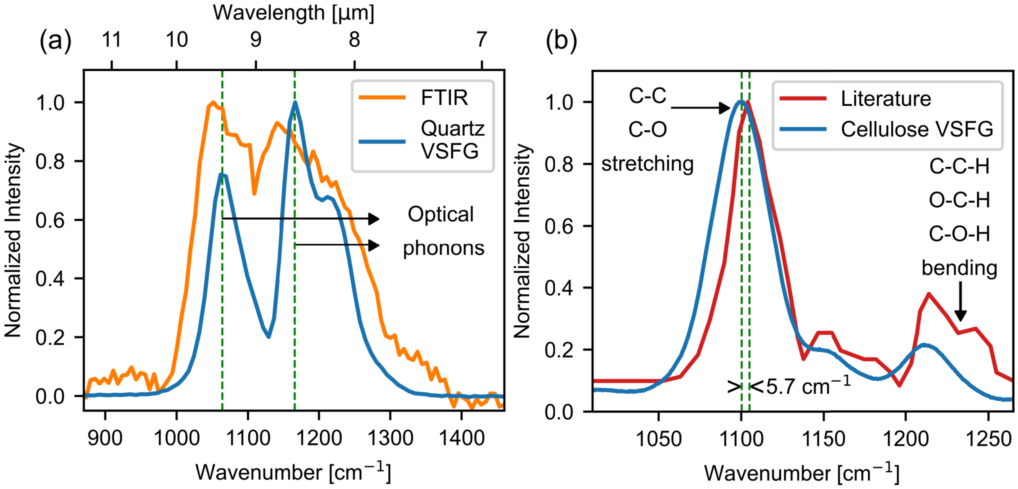

Fig. 4. (a) FTIR spectrum of broadband 9 μm pulses (orange line) and the SFG-response spectrum generated from the quartz surface and measured in reflection mode (blue line). Vertical doted lines mark the characteristic optical phonon modes of quartz [34]. The spectral resolution of the VSFG and the FTIR spectrometer is 32 cm^{-1} and 2 cm^{-1}, respectively. (b) The cellulose VSFG spectrum (red line, adapted from reference [13] compared to our measurement (blue line) allows for precise wavenumber calibration of the VSFG spectrometer (+5.7 cm^{-1}) indicated by shifted vertical dotted green lines. Arrows mark characteristic vibrational modes excited in the cellulose sample [13].

with a diameter of 10 mm and a thickness of 2 mm. In order to prevent damage to the cellulose sample, the power levels for pumping at 515 nm and in the MID-IR are constrained to 50 mW and 10 mW, respectively. A comparative analysis between the cellulose VSFG spectra recorded in our experiments and the published data [13] for calibration is depicted in Fig. 4(b). The vibrational modes in the range from 1000 to 1250 cm^{-1} are attributed to various C-C and C-O stretching modes, as well as C-C-H, O-C-H, and C-O-H bending modes. Notably, the observed peak at 1100 cm^{-1} exhibits distinct sharpness and serves as a valuable spectral reference. By using a Lorentz model to fit this peak, two specific wavenumbers from our measurement and the literature can be determined. Ultimately, our wavenumber axis can be shifted by +5.7 cm^{-1} to align with the 1106 cm^{-1} peak position from the literature for accurate calibration.

3.3. VSFG spectrum of glucose pellets

Table 1. Lorentz fitting parameters, i.e., resonant frequency, natural line width (FWHM), and amplitude of the VSFG spectrum from glucose pellets

Parameters	C-O stretch	C-O stretch	C-O-H bend	CH$_2$ twist	CH$_2$ twist
Freq. [cm^{-1}]	1016	1077	1148	1211	1265
Width [cm^{-1}]	33	38	50	27	34
Amp. [a. u.]	4120	4980	12880	2250	1110

Glucose is the most abundant monosaccharide on earth with the molecular formula $C_6H_{12}O_6$. The naturally occurring stereoisomer of glucose is D-glucose. Its powder (Sigma-Aldrich) utilized in our experiments is hand-pressed into a pellet with a diameter of 10 mm and a thickness

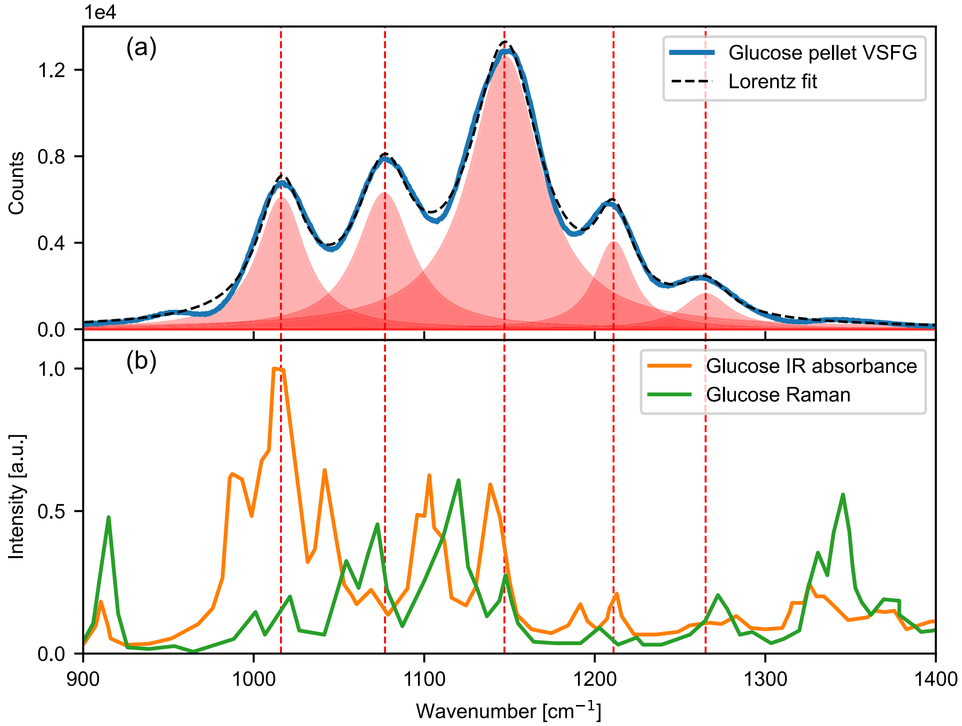

Fig. 5. (a) Recorded VSFG spectrum from glucose pellets (blue line) fitted with Lorentian functions (dotted black line). The observed resonances (light red areas) can be assigned to (b) certain vibrational modes from published IR and Raman spectra indicated by red dashed vertical lines [40,41].

of 2 mm. To prevent the glucose surface from melting, the excitation power levels in the visible at 515 nm and in the MID-IR are restricted to 50 mW and 40 mW, respectively. A distinct cumulative VSFG spectrum is obtained with an exposure time of 30 seconds repeated five times. It is shown in Fig. 5(a), displaying 5 prominent maxima (vibrational modes) indicating that the VSFG setup has a broad spectral detecting range spanning from 900 to 1400 cm^{-1} and provides a very good signal-to-noise ratio, i.e. exhibit high sensitivity. Based on the quartz and FTIR reference spectra shown in Fig. 4(a), optimal probing of molecular fingerprints ranges from 1000 to 1300 cm^{-1}. Notably, the observed VSFG glucose bands coincide with IR and Raman active modes, as shown by red dashed lines in Fig. 5(b), because the VSFG signal results from IR transitions and Raman activity acting as an enhancement factor according to Eq. (1). By referring to the literature [38,39], the observed VSFG bands can be easily assigned, as detailed in Tab. 1.

A common method to determine the intrinsic amplitudes of vibrational modes is to divide the VSFG spectrum by a reference spectrum. However, this approach has not been applied here, because of the central dip in the MID-IR spectral pulse profile and the observed phonon bands in the quartz SFG response spectrum. In particular, weak vibrational structures might be obscured by noise at the processed spectrum's rising and falling edges, where the MID-IR pulse spectral intensity is close to zero. As described in the introductory section, the observed vibrational modes from 1000 to 1200 cm^{-1} were employed to detect low concentrations of glucose in aqueous solutions. Specifically, the C-O stretching mode at 1016 cm^{-1} is IR sensitive [4], while the C-O-H bending mode at 1148 cm^{-1} is Raman-active [5], making them important indicators for monitoring the changes in the VSFG yield of aqueous glucose depending on its concentration.

3.4. VSFG spectra of glucose in aqueous solutions

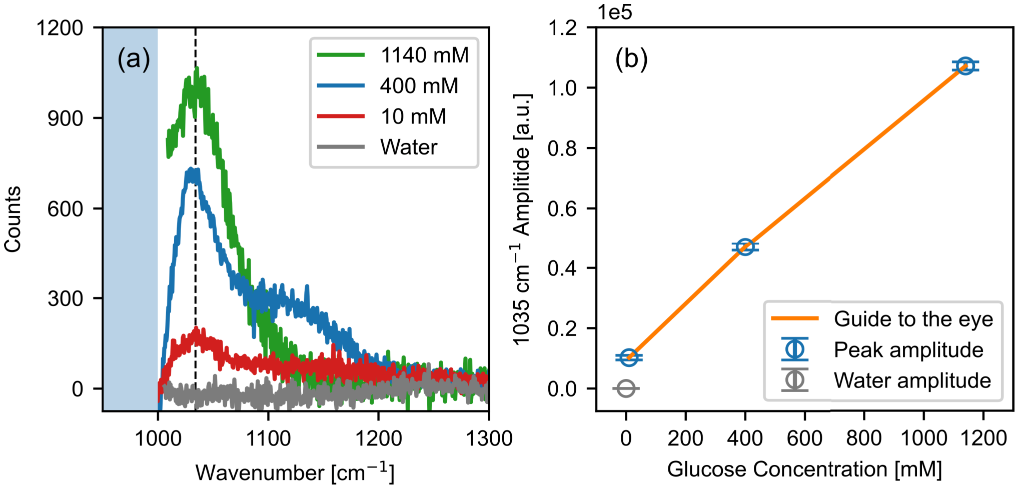

Fig. 6. (a) Recorded VSFG spectra from aqueous glucose for different concentrations (1140, 400, and 10 mM) of the solute in the transmission mode of signal detection. The spectral range < 1000 cm^{-1} affected by background signal from the visible pump on the spectrometer is indicated in blue and the pure water solvent spectrum is shown in gray. (b) The Lorentzian amplitude of the 1035 cm^{-1} C-O stretch vibration indicated in (a) by the dashed vertical line is given as a function of glucose concentrations. The solid line is a guide to the eye.

Different concentrations (1140, 400, and 10 mM) of the solute are prepared by dissolving different amounts of glucose powder in 100 ml of deionized water. A liquid cell (Specac Ltd.) is used to sandwich the solution between two BaF_2 windows with a 5 mm thick spacer. Note, IR spectroscopy on aqueous glucose is challenging, because of the high absorption cross-section of liquid water. Here, we make use of the high transparency of water in the spectral region of interest from 480 to 492 nm, which allows for measuring the transmitted SFG signal. However, since BaF_2 is hydroscopic, the window transparency decreases over time, i.e. the SFG signal drops. This requires two changes in the experimental protocol compared to the reference measurements on solids discussed above. First, higher power levels of visible and MID-IR pulses at 1 W and 120 mW, respectively, are used. Second, a longer exposure time of 30 min is applied. Since the high intensity 515 nm pulse leaks to some extend through the bandpass filter, which discriminates the rather weak SFG signal from the pump, the spectrum below 1000 cm^{-1} is spoiled and not taken into account in the VSFG analysis.

Figure 6(a) displays the derived VSFG spectra for different glucose solutions covering 3 orders of magnitude in concentration between 10 and 1000 mM. All VSFG spectra show the distinct vibration at 1035 cm^{-1}, corresponding to the C-O stretching mode of aqueous glucose [4]. To confirm that the observed vibrational structure originates from the $C_6H_{12}O_6$ solute a spectrum recorded for the pure water solvent is shown in gray. The data indicate that the SFG signal of water at the BaF_2 interface is at or near the noise background level. It is important to note that some dissolution is expected, when a BaF_2 surface is exposed to liquid water. Experiments carried out by Khatib et al. could show how the pH value of water affects the recorded VSFG signal from a similar CaF_2/water interface in the spectral range from 2800 to 3200 cm^{-1} [42]. At low pH, a positively charged fluoride vacancy $(FCa^+)_{surf}$ is created at the crystal surface because of the excess of hydronium ions. At high pH, the hydroxide ions are expected to react with CaF_2 leading to $(CaFOH)_{interf}$ at the interface. However, at neutral pH the interface carries little charge as only a minor amount of CaF_2 will dissolve and the VSFG signal vanishes as the result of a more random orientation of the interfacial water molecules [42]. This is consistent with our measurements, where we don't observe SFG signal from the BaF_2/water interface between 900 and 1400 cm^{-1}. In Fig. 6(b) we plot the recorded VSFG signal (number of counts) integrated over the peak area as a function of concentration. It is worthy to mention that glucose adsorption on the BaF_2 window could form Ba-O and hydrogen bonds at the solid-liquid interface of the liquid cell [43]. Thus, we cannot exclude that the signal strength of the C-O stretch vibration could be affected to some extent by both, the glucose concentration and adsorption at the interface. In any case, our data clearly demonstrates that the VSFG peak can be employed for detecting low glucose concentrations in aqueous solution with high sensitivity. The data benchmark the performance of the spectrometer for spectral fingerprinting of low-concentration specimen at complex interfaces.

4. Conclusion

Vibrational fingerprints of glucose molecules in aqueous solution have been traced by ultra-broadband vibrational sum-frequency generation (VSFG) spectroscopy at physiologically relevant concentrations in the 10 mM range. The VSFG spectrometer exhibits a wide detecting range from 900 to 1400 cm^{-1}. The key-technology component allowing for biologically relevant applications in aqueous solutions is a home-built MID-IR OPCPA laser architecture based on a $LiGaS_2$ nonlinear crystal. The system offers a broadband pulse centered at 9 μm with 114 fs pulse duration and exhibits a high average power of 245 mW and a pulse energy of 1.2 μJ at a pulse repetition rate of 200 kHz. More detailed studies on biomolecules in the fingerprint region will become possible by further developing the technique towards time-resolved VSFG spectroscopy and VSFG microscopy, which we are currently working on. Here, we would like to refer to the impressive work by F. Krausz et al. on field-resolved infrared spectroscopy of biological systems [44]. They could show that time-domain, nonlinear-conversion-based gating of the sampled electric field, which propagates native blood serum, pushes the limit of detecting changes in concentration of individual molecules into the range of hundreds of nanograms per millilitre recorded in less than one minute of data acquisition time. We are convinced that further research and development in this field could pave the way to an all-optical, minimally-invasive and label-free diagnostic in health monitoring. Last but not least, the detection of an unknown low-concentration specimen at complex interfaces opens the door for a wide range of applications in science and industry, e.g. understanding molecular mechanism in heterogeneous catalysis or in bacterial biofilm formation.

Funding. Deutsche Forschungsgemeinschaft (EXC 2056 - project ID 390715994); European Regional Development Fund; Hamburgische Investitions- und Förderbank (IFB); Free and Hanseatic City of Hamburg (Supernova DFG).

Acknowledgments. We thank Dr. A. Przystawik and Class 5 Photonics GmbH for fruitful discussions and support.

Disclosures. The authors declare no conflicts of interest.

Data availability. Data underlying the results presented in this paper are not publicly available at this time but may be obtained from the authors upon reasonable request.

References

1. M. Huber, K. V. Kepesidis, L. Voronina, *et al.*, "Infrared molecular fingerprinting of blood-based liquid biopsies for the detection of cancer," eLife **10**, 68758 (2021).
2. J. Chen and H. Furukawa, "Rapid and non-invasive detection of high-thickness glucose solution concentrations using quantum cascade laser-based transmission infrared spectroscopy," Infrared Phys. Technol. **131**, 104717 (2023).
3. A. Aldoss, R. Lambarte, and F. Alsalleeh, "High-glucose media reduced the viability and induced differential pro-inflammatory cytokines in human periodontal ligament fibroblasts," Biomolecules **13**(4), 690 (2023).
4. J.-J. Max and C. Chapados, "Glucose and fructose hydrates in aqueous solution by IR spectroscopy," J. Phys. Chem. A **111**(14), 2679–2689 (2007).
5. A. Golparvar, A. Boukhayma, T. Loayza, *et al.*, "Very selective detection of low physiopathological glucose levels by spontaneous Raman spectroscopy with univariate data analysis," BioNanoSci. **11**(3), 871–877 (2021).

6. K. E. Shafer-Peltier, C. L. Haynes, M. R. Glucksberg, *et al.*, "Toward a glucose biosensor based on surface-enhanced Raman scattering," J. Am. Chem. Soc. **125**(2), 588–593 (2003).
7. S. Chattopadhyay, M.-S. Li, P. K. Roy, *et al.*, "Non-enzymatic glucose sensing by enhanced Raman spectroscopy on flexible "as-grown" CVD graphene," Analyst **140**(12), 3935–3941 (2015).
8. X. Wang, A. Zhang, M. Zhi, *et al.*, "Glucose concentration measured by the hybrid coherent anti-StokesRaman-scattering technique," Phys. Rev. A **81**(1), 013813 (2010).
9. A. Golparvar, A. Boukhayma, C. Enz, *et al.*, "Rapid, sensitive and selective optical glucose sensing with stimulated Raman scattering (SRS)," in *International Symposium on Medical Measurements and Applications* (IEEE, 2022), pp.1–5.
10. N. I. Cabello, S. Ozawa, S. Kusama, *et al.*, "Background-free mid-infrared absorption spectroscopy using sub-cycle pulses," Opt. Express **32**(16), 27670–27681 (2024).
11. M. Huber, W. Schweinberger, M. Trubetskov, *et al.*, "Detection sensitivity of field-resolved spectroscopy in the molecular fingerprint region," in *CLEO/Europe-EQEC* (2017), p.1.
12. Y. Zhao, S. Kusama, Y. Furutani, *et al.*, "High-speed scanless entire bandwidth mid-infrared chemical imaging," Nat. Commun. **14**(1), 3929 (2023).
13. C. M. Lee, K. Kafle, S. Huang, *et al.*, "Multimodal broadband vibrational sum frequency generation (MM-BB-V-SFG) spectrometer and microscope," J. Phys. Chem. B **120**(1), 102–116 (2016).
14. D. E. Gragson and G. L. Richmond, "Investigations of the structure and hydrogen bonding of water molecules at liquid surfaces by vibrational sum frequency spectroscopy," J. Phys. Chem. B **102**(20), 3847–3861 (1998).
15. G. L. Richmond, "Molecular bonding and interactions at aqueous surfaces as probed by vibrational sum frequency spectroscopy," Chem. Rev. **102**(8), 2693–2724 (2002).
16. X. D. Zhu, H. Suhr, and Y. R. Shen, "Surface vibrational spectroscopy by infrared-visible sum frequency generation," Phys. Rev. B **35**(6), 3047–3050 (1987).
17. H.-F. Wang, L. Velarde, W. Gan, *et al.*, "Quantitative sum-frequency generation vibrational spectroscopy of molecular surfaces and interfaces: Lineshape, polarization, and orientation," Annu. Rev. Phys. Chem. **66**(1), 189–216 (2015).
18. S. M. Baumler and H. C. Allen, "Vibrational spectroscopy of gas–liquid interfaces," in *Physical Chemistry of Gas-Liquid Interfaces*, J. A. Faust and J. E. House, eds. (Elsevier Inc., 2018), Developments in Physical and Theoretical Chemistry, Chap. 5, pp.105–133.
19. A. M. Briggs, M. S. Johal, P. B. Davies, *et al.*, "Structure and thermal stability of dichain sugar surfactants at the solid/water interface studied by sum-frequency vibrational spectroscopy," Langmuir **15**(5), 1817–1828 (1999).
20. H. C. Hieu, H. Li, Y. Miyauchi, *et al.*, "Wetting effect on optical sum frequency generation (SFG) spectra of d-glucose, d-fructose, and sucrose," Spectrochim. Acta, Part A **138**, 834–839 (2015).
21. R. Danilevičius, A. Zaukevičius, R. Kananavičius, *et al.*, "Novel OPCPA based source for broadband high resolution sum frequency generation spectroscopy," in *CLEO/Europe-EQEC* (2017), p. 1.
22. L. Isaenko, A. Yelisseyev, S. Lobanov, *et al.*, "Growth and properties of $LiGaX_2$ (X = S, Se, Te) single crystals for nonlinear optical applications in the mid-IR," Cryst. Res. Technol. **38**(3-5), 379–387 (2003).
23. M. Namboodiri, C. Luo, G. Indorf, *et al.*, "Optical properties of Li-based nonlinear crystals for high power mid-IR OPCPA pumped at 1 μm under realistic operational conditions," Opt. Mater. Express **11**(2), 231–239 (2021).
24. Z. Heiner, L. Wang, V. Petrov, *et al.*, "Broadband vibrational sum-frequency generation spectrometer at 100 kHz in the 950-1750 cm^{-1} spectral range utilizing a $LiGaS_2$ optical parametric amplifier," Opt. Express **27**(11), 15289–15297 (2019).
25. M. Namboodiri, C. Luo, G. F. H. Indorf, *et al.*, "Versatile few-cycle high-energy MID-IR OPCPA for nonlinear optics, spectroscopy and imaging," Opt. Continuum **1**(5), 1157–1164 (2022).
26. J.-M. Cao, A.-A. Liu, S.-Y. Yang, *et al.*, "Vibrational spectra of liquid interfaces with a 100 kHz sub-1 cm^{-1} high-resolution broadband sum-frequency generation vibrational spectrometer (HR-BB-SFG-VS)," J. Phys. Chem. C **127**(28), 14013–14022 (2023).
27. B. M. Luther, K. M. Tracy, M. Gerrity, *et al.*, "2D IR spectroscopy at 100 kHz utilizing a mid-IR OPCPA laser source," Opt. Express **24**(4), 4117–4127 (2016).
28. P. Donaldson, G. Greetham, D. Shaw, *et al.*, "A 100 kHz pulse shaping 2D-IR spectrometer based on dual Yb:KGW amplifiers," J. Phys. Chem. A **122**(3), 780–787 (2018).
29. Y. V. Aulin, A. Tuladhar, and E. Borguet, "Ultrabroadband mid-infrared noncollinear difference frequency generation in a silver thiogallate crystal," Opt. Lett. **43**(18), 4402–4405 (2018).
30. L. J. Richter, T. P. Petralli-Mallow, and J. C. Stephenson, "Vibrationally resolved sum-frequency generation with broad-bandwidth infrared pulses," Opt. Lett. **23**(20), 1594–1596 (1998).
31. M. A. Jakob, M. Namboodiri, M. J. Prandolini, *et al.*, "Generation and characterization of tailored MIR waveforms for steering molecular dynamics," Opt. Express **27**(19), 26979–26988 (2019).
32. A. Yelisseyev, M. Starikova, L. Isaenko, *et al.*, "Effect of post-growth annealing on the optical properties of $LiGaS_2$ nonlinear crystals," in *Nonlinear Frequency Generation and Conversion: Materials, Devices, and Applications X*, vol. 7917 K. L. Vodopyanov, ed., International Society for Optics and Photonics (SPIE, 2011), p. 79171S.
33. J. D. Pickering, M. Bregnhøj, A. S. Chatterley, *et al.*, "Tutorials in vibrational sum frequency generation spectroscopy. II. Designing a broadband vibrational sum frequency generation spectrometer," Biointerphases **17**(1), 011202 (2022).
34. W.-T. Liu and Y. R. Shen, "Sum-frequency phonon spectroscopy on α-quartz," Phys. Rev. B **78**(2), 024302 (2008).

35. X.-H. Hu, F. Wei, H. Wang, *et al.*, "α-quartz crystal as absolute intensity and phase standard in sum-frequency generation vibrational spectroscopy," J. Phys. Chem. C **123**(24), 15071–15086 (2019).
36. M. Makarem, C. M. Lee, K. Kafle, *et al.*, "Probing cellulose structures with vibrational spectroscopy," Cellulose **26**(1), 35–79 (2019).
37. L. Velarde and H.-F. Wang, "Unified treatment and measurement of the spectral resolution and temporal effects in frequency-resolved sum-frequency generation vibrational spectroscopy (SFG-VS)," Phys. Chem. Chem. Phys. **15**(46), 19970–19984 (2013).
38. M. V. Korolevich, R. G. Zhbankov, and V. V. Sivchik, "Calculation of absorption band frequencies and intensities in the IR spectrum of α-d-glucose in a cluster," J. Mol. Struct. **220**, 301–313 (1990).
39. M. Dudek, G. Zajac, E. Szafraniec, *et al.*, "Raman optical activity and Raman spectroscopy of carbohydrates in solution," Spectrochim. Acta, Part A **206**, 597–612 (2019).
40. P. J. Linstrom and W. G. Mallard, *NIST Chemistry WebBook, NIST Standard Reference Database Number 69* (National Institute of Standards and Technology, 2024).
41. S. Söderholm, Y. H. Roos, N. Meinander, *et al.*, "Raman spectra of fructose and glucose in the amorphous and crystalline states," J. Raman Spectrosc. **30**(11), 1009–1018 (1999).
42. R. Khatib, E. H. G. Backus, M. Bonn, *et al.*, "Water orientation and hydrogen-bond structure at the fluorite/water interface," Sci. Rep. **6**(1), 24287 (2016).
43. D. Jin, R. Sun, G. Wang, *et al.*, "Flotation separation of fluorite and calcite using anhydrous glucose and aluminum sulfate as a combined depressant," Appl. Surf. Sci. **624**, 157089 (2023).
44. I. Pupeza, M. Huber, M. Trubetskov, *et al.*, "Field-resolved infrared spectroscopy of biological systems," Nature **577**(7788), 52–59 (2020).